https://doi.org/10.1016/j.energy.2023.128934

A 3D modelling study on all vanadium redox flow battery at various operating temperatures

Qijiao He [a, 1], Zheng Li [a, 1], Dongqi Zhao [a], Jie Yu [a], Peng Tan [b], Meiting Guo [a], Tianjun Liao [c], Tianshou Zhao [d,*], Meng Ni [a,*]

[a] Department of Building and Real Estate, Research Institute for Sustainable Urban Development (RISUD) & Research Institute for Smart Energy (RISE), The Hong Kong Polytechnic University, Hung Hom, Kowloon, Hong Kong, China

[b] Department of Thermal Science and Energy Engineering, University of Science and Technology of China (USTC), Hefei 230026, Anhui, China

[c] Department of Physics and Energy, Chongqing Key Laboratory of Green Energy Materials Technology and Systems, Chongqing University of Technology, Chongqing 400054, China

[d] Department of Mechanical and Energy Engineering, Southern University of Science and Technology, Shenzhen 518055, China

[1] Qijiao He and Zheng Li equally contributed to this work.

[*] Corresponding authors: zhaots@sustech.edu.cn (Tianshou Zhao); meng.ni@polyu.edu.hk (Meng Ni)

Abstract

To understand whether the optimization of the operating/electrode structural parameters are temperature dependent, a 3D numerical model is developed and validated to gain insight into the impact of practical operating temperature (273.15 K~323.15 K) on vanadium redox flow battery (VRFB) performance, in which the property parameters are from published experimental data. The operating temperature is found significantly influence the optimal design of VRFBs. Increasing the inlet flow rate and state of charge (SOC), decreasing the electrode porosity and fibre diameter can all improve the battery performance with interdigitated flow channels, and the improvement increases with increasing temperature. In contrast, decreasing the fibre diameter or porosity increases the flow resistance and costs higher pump consumption, which is more pronounced at a lower temperature due to higher electrolyte viscosity. The effect of electrode thickness is also different at various temperatures. The gradient porosity electrode is applied in VRFB with interdigitated flow channels. The electrochemical performance of VRFB with gradient electrode (porosity increases from 0.8 at channel side to 0.93 at membrane side) performs similarly with the VRFB with 0.8 porosity electrode, while the pressure drop is reduced by 40% at all temperature. This model provides a deep understanding of effects of a wide range of working temperature on the optimization of operating/electrode parameters and on the VRFBs' performance.

Keywords

Vanadium redox flow battery; Numerical modelling; Temperature effects; Parametric study; Structural optimization.

1. Introduction

For realizing carbon neutrality, wind and solar energy as renewable energy have attracted the attention of the industry and scientific research community. But both wind and solar power are intermittent and fluctuating, leading to long-term energy supply instability [1–3]. When their scale is kW to MW, they can be directly integrated into the grid. However, for scale larger than MW, the grid tolerance capacity becomes a problem [4]. To circumvent this problem, long-term energy storage technologies are thus needed to moderate the wind/solar and the grid. As a novel energy storage technology, flow batteries have received growing attentions due to their safety, sustainability, long-life circles and excellent stability. All vanadium redox flow battery (VRFB) is a promising candidate, especially it is the most mature flow battery at the current stage [5]. Fig.1 shows the working principle of VRFB. The VRFBs realize the conversion of chemical energy and electrical energy through the reversible redox reaction of active redox couples in positive and negative electrolyte solutions. During charge process, oxidation reaction occurs in the positive electrode to increase the valence state of the active substance, while reduction reaction occurs in the negative electrode to reduce the valence state of the active substance. The electrochemical reactions are proceeded in the opposite directions in the discharge process. Voltage losses and pump energy consumption are the two most important factors limiting the performance of VRFBs [6].

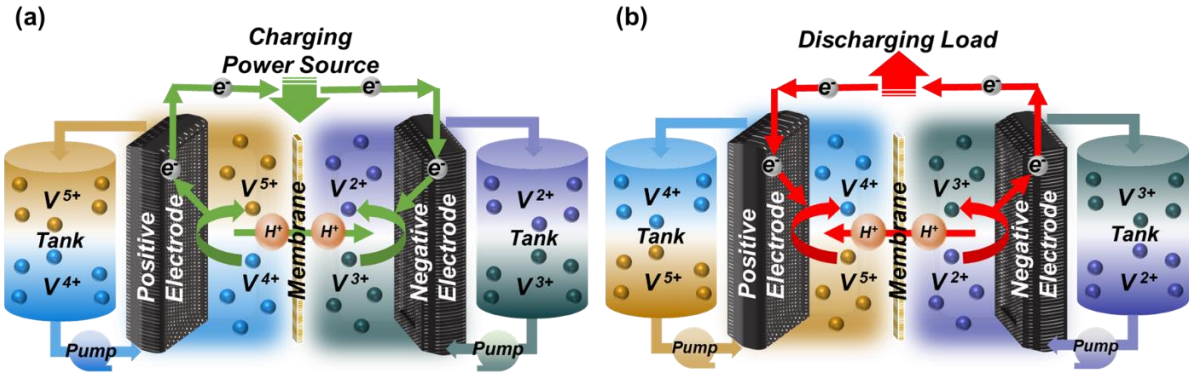

Fig.1 VRFB working principle during charging process (a) and discharging process (b).

Temperature is one of most important parameters affecting VRFBs' performance as it directly affects the electrochemical reactions kinetics and the electrolyte material properties. In practice, VRFBs may need to work at varied temperatures. On the one hand, some places with abundant wind or solar energy, such as deserts, may have large temperature differences between day and night. Therefore, a wide working temperature range enables VRFBs to be installed in situ near wind/solar power plants, further reducing unnecessary losses. On the other hand, temperatures in winter (i.e., 0 ^{o}C or even lower) and summer (i.e. 35 ^{o}C) are substantially different in most places. A wide working temperature range enables VRFBs to operate efficiently in both summer and winter. In recent years, some researchers studied the temperature effects on electrolyte properties of VRFB and tested the performance of single cell in a broad temperature range, which provides very necessary data basis and reference for future research and development. Xiao et al. [7] investigated both the physical and electrochemical properties of vanadium electrolytes from 233.15 K to 323.15 K. The positive electrolyte is found to be stable at a low temperature, while the negative electrolyte behaves more stably at a high temperature. The viscosity of both positive and negative electrolytes decreases while the conductivity increases with the increasing temperature. They also confirmed the enhanced electrochemical activity at a higher temperature. Their follow-up study [8] evaluated the effects of temperature on single cell performance. The results indicate that the energy efficiency of the VRFB can reach 65%~78% at 100 mA cm^{-2} at 253.15 K~323.15 K. Zhang et al. [9] tested a lab-scale single cell through changing ambient temperature to understand the effects of temperature on VRFB. When the temperature increases from 288.15 K to 328.15 K, the peak power density increases from 259.5 mW cm^{-2} to 349.8 mW cm^{-2}, and the voltage efficiency increases from 86.5% to 90.5% at 40 mA cm^{-2}. Yin et al. [10] focused on the ion transfer processes in VRFB at 283.15 K~323.15 K and discussed the temperature dependence of the ion transfer properties. Further, they gave a temperature effects route map to clarify the relation between battery

performance and ions mass transfer properties. The research group of the University of New South Wales carried out lots of very valuable works since they successfully built first VRFB [11]. They developed an empirical model considering the linear dependence of electrolyte conductivity on the electrolyte temperature and state of charge (SOC) to detect system imbalance [12]. However, Ressel et al. [13] applied a different approach to estimate SOC by using temperature corrected in-situ electrolyte density measurements of VRFB.

Some researchers also tested and analysed the VRFBs with optimized material and structure at different temperatures. Kim et al. [14] reported that sodium formate can act as a promising additive for VRFB to achieve high performance with high-temperature tolerance by preventing precipitation and decreasing viscosity of the electrolyte. The applicability of several typical membranes to VRFB at different temperatures is evaluated by Xi et al. [15]. Rao et al. [16] investigated how to restore the lost discharge capacity and energy efficiency at low temperature (263.15K and 283.15K) by applying thinner electrode and increasing the electrode compression ratio.

Moreover, the visualization of VRFB characteristics by simulation is an essential tool to better understand the cell charge and discharge processes, design optimized structure and save both time and money compared with experiment [17]. VRFB thermal model is an essential tool for studying the behaviour of the battery and optimizing its performance, efficiency, lifespan, and safety. Some researchers developed thermal model of VRFB to further study the effects of operating conditions on heat generation at room temperature, which is also beneficial to the establishment of battery management system (BMS) [18–20]. For larger VRFB scale, some stack and system models for the study of thermal effects were proposed to investigate the overall performance and efficiency of the batteries, considering the flow pattern [21] or shunt current losses [22]. Wang et al. [23] built a thermal model to study the steady and dynamic-state thermal conditions of VRFB system and proposed the improved cooling strategy to save

air conditioner consumption. The modelling methods of life-cycle charging state of VRFB considering the change of current and temperature can be referred to lithium-ion batteries studies from Wang et al. [24]. They also proposed the improved anti-noise adaptive neural network for accurate battery remaining useful life prediction [25], which provides a reference for the VRFB lifespan model. The above simulations are mostly based on room temperature. Different temperatures have great influence on the electrolyte properties and the electrochemical reaction rate, so it is also very important to establish the battery temperature effects model, which can help researchers better predict the battery performance. Xu et al. [26] built numerical model of iron-vanadium redox flow battery with deep eutectic solvent electrolyte and studied the temperature effects on over-potential and pumping loss. Some researchers also proposed numerical models to study the effects of electrode porosity [27], electrolyte concentration [28], flow pattern [29] and membrane [30] on VRFB performance, but all of them were carried out at room temperature.

The above-mentioned works show great impacts of working temperature on the performance of VRFB. However, most of them are experimental-based studies and cannot give quantitative description of working temperature effects on the complex physical/chemical/electrochemical phenomena in VRFB. The simulation works are still lacking at different temperatures. The relevant understanding is still vague [31–33]. To fill the research gap, a three-dimensional model is developed to investigate the effects of operating and electrode structural parameters on the VRFB performance over a wide range of temperature, from 273.15 K to 323.15 K. The model delivers detailed understanding of how temperature affects optimization of operating/electrode structural parameters, thereby minimizing the voltage losses and pump energy consumption. Such a model provides valuable information on how to formulate corresponding operating strategies for different working temperatures and how to optimize electrode fabrication at different temperature ranges. Furthermore, this model can serve as a

useful tool for VRFB design and offer valuable insights for other flow batteries with similar physical and electrochemical properties.

2. Methods

A 3D model is built for a VRFB with interdigitated flow field. Details can be found in Fig.2. The interdigitated flow field is applied in VRFB to 1) decrease the ohmic loss; 2) save the pump power; 3) supply the reactants uniformly in the electrolyte. Zero potential is applied at the contact surface of the current collector and the negative porous electrode. The working voltage, from open-circuit voltage (OCV) to 0.15 V, is applied to the contact surface of the current collector and the positive electrode to calculate the according current density (polarization curves). The whole battery is shown in Fig.2 (a), which has a 400 mm^2 active square electrode on each side. Due to similar mass transfer process between the adjacent channels, the unit computational domain is applied. The unit computational domain consists of a 2 mm×16 mm active electrode and half inflow/outflow channels which are symmetrical along the centre line on each side, as shown in Fig.2 (b).

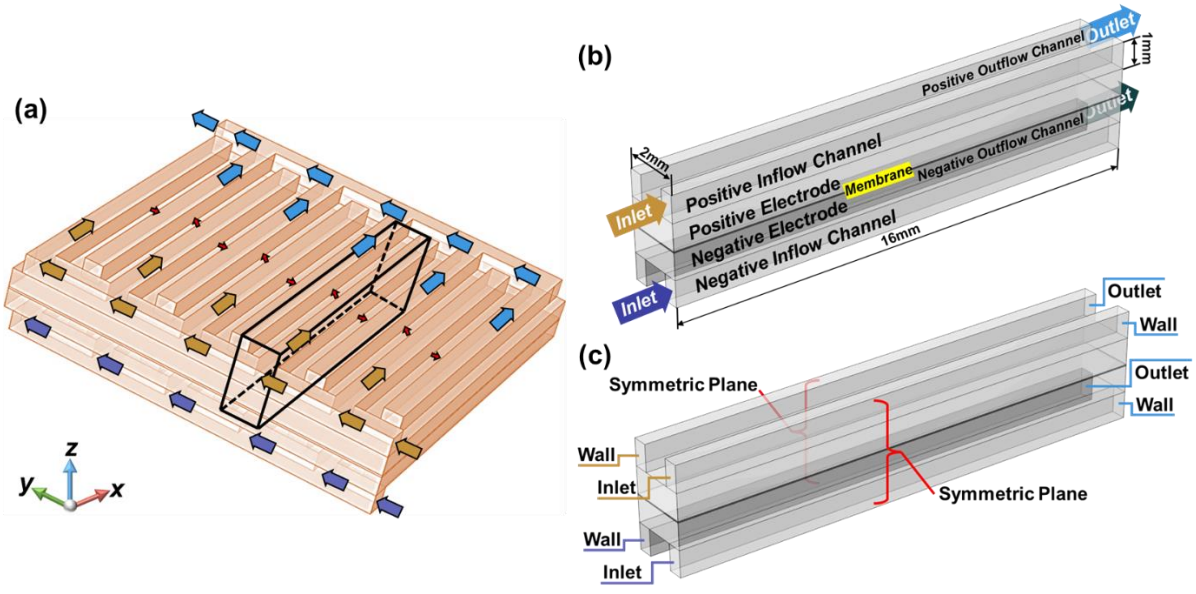

Fig.2 Schematic diagram of the whole battery (a), the unit computational domain (b) and the boundary condition setting (c).

The initial concentration settings in computation refer to the experiment [24]. The process of configuring the electrolyte is as following:

1. Add 0.75 mol V_2O_5 solid powder to 1 L of 3.875 mol H_2SO_4 solution with the chemical reaction, $2H^+ + V_2O_5 \leftrightarrow 2VO_2^+ + H_2O$.

The concentration of H_2SO_4 solution is 3.875 mol L^{-1} (M) at the beginning. After dissolution and reaction, with the assumption that the sulfuric acid is fully dissociated, the solution consists of 1.5 M VO_2^+, 6.25 M H^+, and 3.875 M SO_4^{2-}.

2. In the pre-step, the electrochemical reactions are performed. The reduction reaction is $2VO_2^+ + 3e^- + 6H^+ \leftrightarrow VO^{2+} + V^{3+} + 3H_2O$. The oxidation reaction is $H_2O \leftrightarrow 0.5O_2 + 2H^+ + 2e^-$.

After the pre-step, the solution in the reduction side can be used as the initial electrolyte [7]. The initial electrolyte comprises 0.75 M VO^{2+}, 0.75 M V^{3+}, 4 M H^+ and 3.875 M SO_4^{2-}, which means the initial total vanadium ion concentration, $c_{V_{total}}^0$, is 1.5 M.

3. In the pre-charge step, the positive reaction is $V^{3+} + H_2O \leftrightarrow VO^{2+} + 2H^+ + e^-$. The negative reaction is $VO^{2+} + 2H^+ + e^- \leftrightarrow V^{3+} + H_2O$.

After the pre-step, the SOC of electrolyte is 0, the positive electrolyte consists of 1.5 M VO^{2+}, 4.75 M H^+ and 3.875 M SO_4^{2-} and the negative electrolyte consists of 1.5 M V^{3+}, 3.25 M H^+ and 3.875 M SO_4^{2-}.

At this point, the initial electrolyte configuration is complete and the battery charging and discharging process can proceed. The reactions occurring in negative and positive electrodes of VRFB can be expressed as:

At negative electrode: $V^{2+} \underset{Charge}{\overset{Discharge}{\rightleftharpoons}} V^{3+} + e^-$

At positive electrode: $VO_2^+ + 2H^+ \underset{Charge}{\overset{Discharge}{\rightleftharpoons}} VO^{2+} + H_2O - e^-$

After charge reaction, the SOC is 1, the positive electrolyte consists of 1.5 M VO_2^+, 6.25 M H^+ and 3.875 M SO_4^{2-} and the negative electrolyte consists of 1.5 M V^{2+}, 4.75 M H^+ and 3.875 M SO_4^{2-}.

The inlet species concentration, c_i^{in}, is determined by the SOC_{in} except SO_4^{2-} as constant:

$$c^{in}_{SO_4^{2-}\,pos} = c^{in}_{SO_4^{2-}\,neg} = \left(1\ M + 2.5 \times c^0_{V_{total}}\right)/2 = 3.875\ \text{M}$$

$$c^{in}_{H^+_{neg}} = 4M + (SOC_{in} - 0.5) \cdot c^0_{V_{total}}$$

$$c^{in}_{H^+_{pos}} = 4M + (SOC_{in} + 0.5) \cdot c^0_{V_{total}}$$

$$c^{in}_{VO_2^+} = c^{in}_{V^{2+}} = SOC_{in} \cdot c^0_{V_{total}}$$

$$c^{in}_{VO^{2+}} = c^{in}_{V^{3+}} = (1 - SOC_{in}) \cdot c^0_{V_{total}}$$

2.1 Model assumptions

In the present work, some assumptions are applied as follows:

1. The entire computational domain is isothermal, due to the good thermal conductivity and high heat capacity of liquid electrolyte.

2. The fluid flow is incompressible.

3. The VRFB is in steady state operation, considering that the two external tanks are large enough.

4. The possible side reactions, such as hydrogen and oxygen evolutions, are neglected.

5. Apart from proton transport, the membrane does not allow mass transport or transport of other ions.

2.2 Momentum and mass transport

The mass and the momentum conservation for electrolyte can be expressed with the continuity equation, Navier-Stokes equation, and Brinkman equation, respectively:

$$0 = \rho \nabla \cdot \vec{u} \tag{1}$$

$$-\nabla p + \nabla \cdot [\mu(\nabla \vec{u} + (\nabla \vec{u})^T)] = \rho(\vec{u} \cdot \nabla)\vec{u} \tag{2}$$

$$-\nabla p + \nabla \cdot \left[\frac{\mu}{\varepsilon}(\nabla \vec{u} + (\nabla \vec{u})^T)\right] - \frac{\mu}{\kappa}\vec{u} = \frac{\rho}{\varepsilon^2}(\vec{u} \cdot \nabla)\vec{u} \tag{3}$$

where u is the velocity (m s^{-1}), ρ is the density (mol m^{-3}), p is the pressure (Pa), μ is the dynamic viscosity (Pa·s), ε is the electrode porosity, and κ is the permeability of porous electrode, which is expressed as [25]:

$$\kappa = \frac{\varepsilon^3 d_f^2}{16 k_{ck}(1-\varepsilon)^2} \tag{4}$$

where d_f is the fibre diameter (μm), k_{ck} is the dimensionless Carman-Kozeny constant, which is set to be 4.28 [26].

According to fitting formula of experimental data, the two temperature-dependent parameters, dynamic viscosity [10] and electrolyte density [13], can be determined as follows:

$$\mu_{neg} = \upsilon_{neg} \cdot \rho_{neg} = 8 \times \rho_{neg} \times exp(-0.055 \times (T - T_0) + 1.4) \times (1 - SOC) + \upsilon_{pos} \cdot \rho_{pos} \cdot SOC \tag{5}$$

$$\rho_{neg} = -0.0006\ g \cdot (ml \cdot K)^{-1} \times \left(T - T_{ref}\right) + 1.3686\ g \cdot ml^{-1} \tag{6}$$

$$\mu_{pos} = \upsilon_{pos} \cdot \rho_{pos} = 4.5 \times \rho_{pos} \times exp(-0.06 \times (T - T_0) + 1.6) \tag{7}$$

$$\rho_{pos} = -0.0006\ g \cdot (ml \cdot K)^{-1} \times \left(T - T_{ref}\right) + 1.3447\ g \cdot ml^{-1} \tag{8}$$

where T is the temperature of fluid (K), $T_{ref} = 298.15$ K, $T_0 = 273.15$ K, and υ is the kinetic viscosity of the fluid (m^2 s^{-1}). The specific surface area of the electrode, a, is determined by porosity and fibre diameter as [27]:

$$a = \frac{4(1-\varepsilon)}{d_f} \tag{9}$$

The Nernst-Plank equation [28] is employed to describe the transport of dilute species in the porous electrode which comprises convective, migrative, and diffusive terms:

$$\vec{N_i} = -\frac{z_i c_i D_i^{eff}}{RT} F \nabla \phi_l + \vec{u} c_i - D_i^{eff} \nabla c_i \tag{10}$$

$$\nabla \cdot \vec{N_i} = S_i \tag{11}$$

where the index i represents the species, and $\vec{N}_i$ is the flux of the species (mol m^{-2} s^{-1}). c_i and z_i are molar concentration (mol m^{-3}) and charge number of species i, respectively. F is Faraday constant (96485 C mol^{-1}). ϕ_l is the potential in the electrolyte (V). S_i is the species molar source term (mol m^{-3} s^{-1}) , which represents the generation/consumption rate of species due to the electrochemical reactions.

The effective diffusivity D_i^{eff} (m^2 s^{-1}) is corrected according to the Bruggeman correction [29]:

$$D_i^{eff} = \varepsilon^{3/2} D_i \tag{12}$$

The empirical equation is used based on the linearity of the diffusion coefficients of 1.5 M electrolytes with the temperature and the SOC of vanadium ions [10]:

$$\ln D_{V^{2+},V^{3+}} = -2713.09 \times \left(\frac{1}{T}\right) - 5.67 \times (1 - 0.14 \times SOC - 0.61 \times SOC^2) \tag{13}$$

$$\ln D_{VO^{2+},VO_2^+} = -4122.59 \times \left(\frac{1}{T}\right) - 1.04 \times (1 + 1.27 \times SOC - 5.87 \times SOC^2) \tag{14}$$

2.3 Electrochemistry

In electrochemistry, the general Butler-Volmer equation is used to link the activation overpotential with the current density. Charge transport in the electrode for negative side is solved as:

$$\nabla \cdot \vec{i}_l = -\sigma_l^{eff} \nabla^2 \phi_l = -i_{neg} \tag{15}$$

$$\nabla \cdot \vec{i}_s = -\sigma_s^{eff} \nabla^2 \phi_s = i_{neg} \tag{16}$$

where $\vec{i}_l$ is the current density in the electrolyte (A m^{-2}), $\vec{i}_s$ is the current density in the electrode. ϕ_l and ϕ_s are the ionic potential and electronic potential. σ_l^{eff} and σ_s^{eff} represent the effective ionic and electronic conductivity (S m^{-1}) derived from the following expressions.

$$\sigma_l^{eff} = \varepsilon^{1.5} \sigma_l \tag{17}$$

$$\sigma_s^{eff} = (1 - \varepsilon)^{1.5} \sigma_s \tag{18}$$

The positive electrode has similar equations for charge transport.

$$\nabla \cdot \vec{\imath}_l = -\sigma_l^{eff} \nabla^2 \phi_l = -i_{pos} \tag{19}$$

$$\nabla \cdot \vec{\imath}_s = -\sigma_s^{eff} \nabla^2 \phi_s = i_{pos} \tag{20}$$

The ionic conductivity σ_l is calculated from the empirical equation [12].

$$\sigma_{l,pos} = (1.8 \times (T - T_0) + 93.503) \times SOC + (4.6713 \times (T - T_0) + 172.07) \tag{21}$$

$$\sigma_{l,neg} = (0.705 \times (T - T_0) + 55.042) \times SOC + (2.6176 \times (T - T_0) + 122.37) \tag{22}$$

where $T_0 = 273.15$ K. The unit of conductivity calculated from Eq. (21) and (22) is mS cm^{-1}. The ionic current density at the membrane, i_{mem}, determines the magnitude of the proton flux on membrane surfaces. For negative membrane surface, the proton flux is i_{mem}/F. For positive membrane surface, the proton flux is $-i_{mem}/F$. The membrane is modeled by using Ohm's law.

$$\nabla \cdot \vec{\imath}_l = -\sigma_m \nabla^2 \phi_l = -i_{mem} \tag{23}$$

where the σ_m is the membrane conductivity.

The source term S_i of different species i is related to the electrochemical reaction rate i_{neg} and i_{pos}. For the negative electrode: $S_{V^{3+}} = -i_{neg}/F$, $S_{V^{2+}} = i_{neg}/F$. For the positive electrode: $S_{VO_2^+} = -i_{pos}/F$, $S_{VO^{2+}} = i_{pos}/F$, $S_{H^+} = -2i_{pos}/F$. The transfer current density, which is also termed local current density as, i_{loc}, is defined as, i_{neg}/a in negative electrode and i_{pos}/a in positive electrode. The electrochemical reactions occurring on the surfaces of solid fibre in the electrode can be expressed by the Butler-Volmer equation [18]:

$$i_{neg} = aFk_{neg}^0 c_{V^{2+}}^{\alpha_{c,neg}} c_{V^{3+}}^{\alpha_{a,neg}} \left[\frac{c_{V^{3+}}^s}{c_{V^{3+}}} \exp\left(-\frac{\alpha_{c,neg} F \eta_{neg}}{RT} \right) - \frac{c_{V^{2+}}^s}{c_{V^{2+}}} \exp\left(\frac{\alpha_{a,neg} F \eta_{neg}}{RT} \right) \right] \tag{24}$$

$$i_{pos} = aFk_{pos}^0 c_{VO^{2+}}^{\alpha_{c,pos}} c_{VO_2^+}^{\alpha_{a,pos}} \left[\frac{c_{VO_2^+}^s}{c_{VO_2^+}} \exp\left(-\frac{\alpha_{c,pos} F \eta_{pos}}{RT} \right) - \frac{c_{VO^{2+}}^s}{c_{VO^{2+}}} \exp\left(\frac{\alpha_{a,pos} F \eta_{pos}}{RT} \right) \right] \tag{25}$$

where k_{neg}^0 and k_{pos}^0 is the reaction rate constant of the reactions occurring in positive and negative sides, respectively. $\alpha_{c,neg}$ and $\alpha_{a,neg}$ are cathodic and anodic charge transfer coefficient of negative half-reaction, $\alpha_{c,pos}$ and $\alpha_{a,pos}$ are cathodic and anodic charge transfer coefficient of positive half-reaction. R is the ideal gas constant (8.314 J mol^{-1} K^{-1}). c_i^s is the

concentration at the fibre surface of species i. Overpotentials η_{neg} and η_{pos} are defined as follows:

$$\eta_{neg} = \phi_{s,neg} - \phi_{e,neg} - E_{eq,neg} \tag{26}$$

$$\eta_{pos} = \phi_{s,pos} - \phi_{e,pos} - E_{eq,pos} \tag{27}$$

Equilibrium potentials are calculated via:

$$E_{eq,neg} = E^0_{neg} + \frac{RT}{F}\ln\left(\frac{c_{V^{3+}}}{c_{V^{2+}}}\right) \tag{28}$$

$$E_{eq,pos} = E^0_{pos} + \frac{RT}{F}\ln\left(\frac{c_{VO_2^+}c^2_{H^+}}{c_{VO^{2+}}}\right) \tag{29}$$

The standard potentials E^0_{neg} and E^0_{pos} are related to the temperature [19].

$$E^0_{neg} = E^0_{neg,ref} + \left.\frac{dE_0}{dT}\right|_{neg}\left(T - T_{ref}\right) = 1.004 + \frac{\Delta S_{neg}}{nF}\left(T - T_{ref}\right) \tag{30}$$

$$E^0_{pos} = E^0_{pos,ref} + \left.\frac{dE_0}{dT}\right|_{pos}\left(T - T_{ref}\right) = -0.255 + \frac{\Delta S_{pos}}{nF}\left(T - T_{ref}\right) \tag{31}$$

where the $E^0_{neg,ref}$ and $E^0_{pos,ref}$ are the standard equilibrium potentials at $T_{ref} = 298.15$ K. The temperature dependent term for the negative or positive electrode is related to the entropy changes ΔS_{neg} = 21.7 J mol^{-1} K^{-1} and ΔS_{pos} = 100 J mol^{-1} K^{-1} during the electrochemical reactions [30]. n denotes the number of charge transferred in the electrochemical reaction, which value is 1 in the calculation.

The vanadium ions concentration at the surface of carbon fibers can be calculated by balancing the reaction rate and the rate of ion transfer from the bulk to the interface. A quasi-equilibrium state assumption is adopted for the ions transport considering that SOC of electrolyte changes slowly due to relatively small volume of electrolyte in the cell compared with that in the reservoirs. Therefore, the local flux at the surface of the negative electrode is [18]:

$$\begin{aligned} N^S_{V^{2+}} &= k_m\left(c_{V^{2+}} - c^S_{V^{2+}}\right) = -i_{neg}/(aF) \\ &= k^0_{neg} c^{\alpha_{c,neg}}_{V^{2+}} c^{\alpha_{a,neg}}_{V^{3+}} \left[\frac{c^S_{V^{2+}}}{c_{V^{2+}}}\exp\left(\frac{\alpha_{a,neg}F\eta_{neg}}{RT}\right) - \frac{c^S_{V^{3+}}}{c_{V^{3+}}}\exp\left(-\frac{\alpha_{c,neg}F\eta_{neg}}{RT}\right)\right] \\ N^S_{V^{3+}} &= k_m\left(c_{V^{3+}} - c^S_{V^{3+}}\right) = i_{neg}/(aF) \end{aligned} \tag{32}$$

$$= k_{neg}^{0} c_{V^{2+}}^{\alpha_{c,neg}} c_{V^{3+}}^{\alpha_{a,neg}} \left[\frac{c_{V^{3+}}^{s}}{c_{V^{3+}}} \exp\left(-\frac{\alpha_{c,neg} F \eta_{neg}}{RT} \right) - \frac{c_{V^{2+}}^{s}}{c_{V^{2+}}} \exp\left(\frac{\alpha_{a,neg} F \eta_{neg}}{RT} \right) \right] \quad (33)$$

Combining Eqs. (32) and (33), the concentrations of V^{2+} and V^{3+} at the carbon fiber surface are derived as

$$c_{V^{3+}}^{s} = \frac{A_1 c_{V^{2+}} + (1+A_1) c_{V^{3+}}}{1 + A_1 + B_1} \quad (34)$$

$$c_{V^{2+}}^{s} = \frac{B_1 c_{V^{3+}} + (1+B_1) c_{V^{2+}}}{1 + A_1 + B_1} \quad (35)$$

where

$$A_1 = \frac{k_{neg}^{0}}{k_m} c_{V^{2+}}^{\alpha_{c,neg}-1} c_{V^{3+}}^{\alpha_{a,neg}} \exp\left(\frac{\alpha_{a,neg} F \eta_{neg}}{RT} \right) \quad (36)$$

$$B_1 = \frac{k_{neg}^{0}}{k_m} c_{V^{2+}}^{\alpha_{c,neg}} c_{V^{3+}}^{\alpha_{a,neg}-1} \exp\left(\frac{-\alpha_{c,neg} F \eta_{neg}}{RT} \right) \quad (37)$$

the local flux at the surface of the positive electrode is:

$$N_{VO^{2+}}^{s} = k_m \left(c_{VO^{2+}} - c_{VO^{2+}}^{s} \right) = -i_{pos} / (aF)$$

$$= k_{pos}^{0} c_{VO^{2+}}^{\alpha_{c,pos}} c_{VO_2^{+}}^{\alpha_{a,pos}} \left[\frac{c_{VO^{2+}}^{s}}{c_{VO^{2+}}} \exp\left(\frac{\alpha_{a,pos} F \eta_{pos}}{RT} \right) - \frac{c_{VO_2^{+}}^{s}}{c_{VO_2^{+}}} \exp\left(-\frac{\alpha_{c,pos} F \eta_{pos}}{RT} \right) \right] \quad (38)$$

$$N_{VO_2^{+}}^{s} = k_m \left(c_{VO_2^{+}} - c_{VO_2^{+}}^{s} \right) = i_{pos} / (aF)$$

$$= k_{pos}^{0} c_{VO^{2+}}^{\alpha_{c,pos}} c_{VO_2^{+}}^{\alpha_{a,pos}} \left[\frac{c_{VO_2^{+}}^{s}}{c_{VO_2^{+}}} \exp\left(-\frac{\alpha_{c,pos} F \eta_{pos}}{RT} \right) - \frac{c_{VO^{2+}}^{s}}{c_{VO^{2+}}} \exp\left(\frac{\alpha_{a,pos} F \eta_{pos}}{RT} \right) \right] \quad (39)$$

Combining Eqs. (38) and (39), the concentrations of VO^{2+} and VO_2^{+} at the carbon fiber surface are derived as

$$c_{VO_2^{+}}^{s} = \frac{A_2 c_{VO^{2+}} + (1+A_2) c_{VO_2^{+}}}{1 + A_2 + B_2} \quad (40)$$

$$c_{VO^{2+}}^{s} = \frac{B_2 c_{VO_2^{+}} + (1+B_2) c_{VO^{2+}}}{1 + A_2 + B_2} \quad (41)$$

where

$$A_2 = \frac{k_{pos}^{0}}{k_m} c_{VO^{2+}}^{\alpha_{c,pos}-1} c_{VO_2^{+}}^{\alpha_{a,pos}} \exp\left(\frac{\alpha_{a,pos} F \eta_{pos}}{RT} \right) \quad (42)$$

$$B_2 = \frac{k_{pos}^{0}}{k_m} c_{VO^{2+}}^{\alpha_{c,pos}} c_{VO_2^{+}}^{\alpha_{a,pos}-1} \exp\left(\frac{-\alpha_{c,pos} F \eta_{pos}}{RT} \right) \quad (43)$$

Based on the Arrhenius law, the reaction rate constants, k_{neg}^{0} and k_{pos}^{0} are temperature dependent and can be written as follows:

$$k_{neg}^{0} = k_{neg,ref}^{0}\exp\left(-\frac{\Delta G_{neg}^{0}}{R}\left(\frac{1}{T_{ref}}-\frac{1}{T}\right)\right) = k_{neg,ref}^{0}\exp\left(\frac{nFE_{neg}^{0}}{R}\left(\frac{1}{T_{ref}}-\frac{1}{T}\right)\right) \quad (44)$$

$$k_{pos}^{0} = k_{pos,ref}^{0}\exp\left(-\frac{\Delta G_{pos}^{0}}{R}\left(\frac{1}{T_{ref}}-\frac{1}{T}\right)\right) = k_{pos,ref}^{0}\exp\left(\frac{nFE_{pos}^{0}}{R}\left(\frac{1}{T_{ref}}-\frac{1}{T}\right)\right) \quad (45)$$

where $\Delta G_{neg}^{0} = -nFE_{neg}^{0}$ and $\Delta G_{pos}^{0} = -nFE_{pos}^{0}$ are the standard Gibbs free energy change for the respective reaction. $k_{neg,ref}^{0}$ and $k_{pos,ref}^{0}$ are the standard reaction rate constants at $T_{ref} = 298.15$ K. The local mass transfer coefficient can be calculated approximately [31]:

$$k_m = 8.85 \times 10^{-4}|\vec{u}|^{0.9} \quad (46)$$

The parameters of geometry, operating conditions, electrochemical reactions and material properties are listed in Table 1 and Table 2.

Table 1 Geometric and operating parameters.

Parameters	Symbols (Unit)	Value
$thick_e$	Electrode thickness (mm)	0.5 ~ 1.5
$thick_m$	Membrane thickness (μm)	50
rib_w	Rib width (mm)	1
$channel_w$	Channel width (mm)	1
$channel_d$	Channel depth (mm)	1
$channel_l$	Channel length (mm)	16
$channel_n$	Inflow channel number	5
ε	Electrode porosity	0.8 ~ 0.93 and gradient
d_f	Carbon electrode fibre diameter (μm)	5 ~ 20 and gradient
V_{work}	Working voltage (V)	Open-circuit voltage (OCV)~ 0.15
SOC_{in}	SOC of inlet	0.2 ~ 0.8
Q_{in}	Inlet flow rate (ml min^{-1})	10 ~ 60
T	Working temperature (K)	273.15 ~ 323.15

Table 2 Electrochemical parameters and material properties.

Parameters	Symbols (Unit)	Value
$E^0_{neg,ref}$	Standard equilibrium potentials of negative side at 298.15 K (V)	-0.255 [32]
$E^0_{pos,ref}$	Standard equilibrium potentials of positive side at 298.15 K (V)	1.004 [32]
$\alpha_{a,neg}$	Anodic charge transfer coefficient for negative side	0.5
$\alpha_{c,neg}$	Cathodic charge transfer coefficient for negative side	0.5
$\alpha_{a,pos}$	Anodic charge transfer coefficient for positive side	0.5
$\alpha_{c,pos}$	Cathodic charge transfer coefficient for positive side	0.5
$k^0_{pos,ref}$	The standard reaction rate constant of negative side (m s^{-1})	6.8×10^{-7} [33]
$k^0_{neg,ref}$	The standard reaction rate constant of negative side (m s^{-1})	1.7×10^{-7} [34]
D_{H^+}	Proton diffusion coefficient (m^2 s^{-1})	9.3×10^{-9} [35]
$D_{SO_4^{2-}}$	SO_4^{2-} diffusion coefficient (m^2 s^{-1})	1.1×10^{-9} [35]
σ_s	Electrode material conductivity (S m^{-1})	5000
σ_m	Membrane conductivity (S m^{-1})	12

2.4 Boundary conditions

The boundary conditions are shown in Fig.2 (c). Working voltage, V_{work}, is applied from OCV to 0.15 V on the contact surface of the positive porous electrode and the current collector. Zero potential is adopted at the contact surface of the negative porous electrode and the current collector, as mentioned above. The inflow velocity boundary of the unit calculational domain is set to be v_{in},

$$v_{in} = \frac{Q_{in}}{channel_n \times 2 \times A_{in}} = \frac{Q_{in}}{channel_n \times 2 \times \frac{channel_w}{2} \times channel_d} \tag{47}$$

where A_{in} is the cross-sectional area of the half inflow channel in the computational domain. Since the calculated inflow channel domain is only half the actual size, the inflow rate Q_{in} also needs to be divided by two. At the outlet of the outflow channel, the pressure is set to be zero

as the reference and concentration gradient is assumed to be zero. The inlet species concentration, c_i^{in}, is given in details at the beginning of this section. The two ends of the unit in the zx-plane are set as symmetric plane in charge transfer, mass, and species. All the other boundaries are impermeable to the charge transfer, mass, and species.

2.5 Validation and case study details

The above equations are solved based on the finite element method. The relative tolerance is set to 1×10^{-4}. The model is validated at inlet flow rate 20 mL min^{-1}, current density 60 mA cm^{-2}, 1.5 M total vanadium ion concentration, 0.06 ~ 0.94 SOC, and ambient temperatures 273.15 K ~ 323.15 K through discharge curves. The simulation results show good agreement with experimental data [10], as shown in Fig.3 (a). The mesh independence check is shown in Fig.3 (b). The number of 414 thousand is chosen for the degrees of freedom in the subsequent simulations.

The porosity of 0.8 ~ 0.93 is chosen for calculation because commercial electrodes generally have a porosity of 0.95. After installation, slight compression is needed for sealing and long-term stability, thus the porosity is lower than 0.93 according to different compression ratio. Further compression of the electrode makes the pump consumption rise rapidly and is possible to crush the membrane in the middle, thus 0.8 is selected as the lower porosity limit for the study.

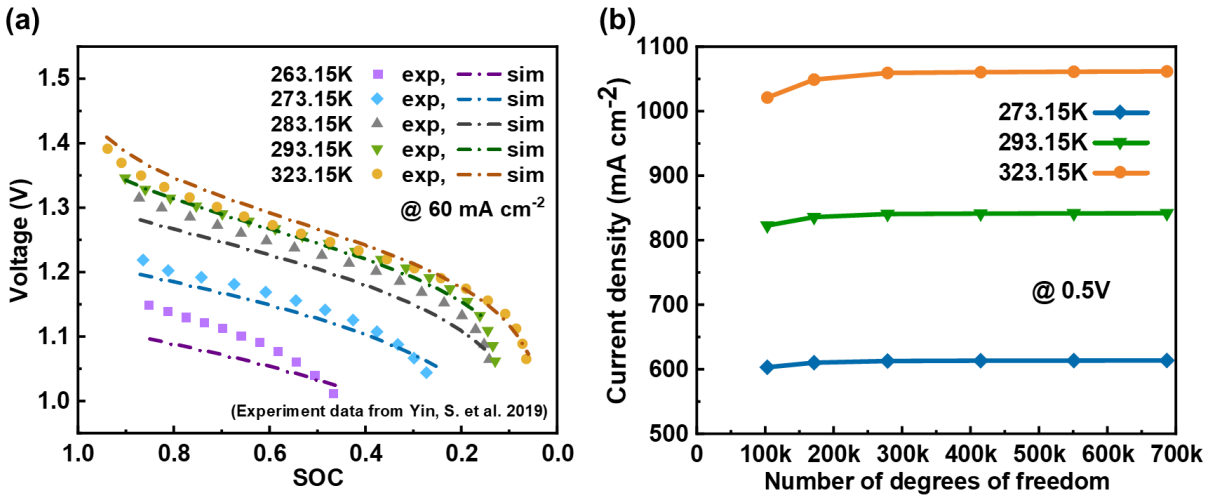

Fig.3 (a) Model validation for the VRFBs working at various temperature; (b) Mesh independence validation.

For investigating the effect of different electrode porosity distributions on electrochemical performance of battery, different gradient electrodes are constructed, as shown in Fig.4. For example, the gradient electrode with decreasing porosity in z-direction means the porosity decreases linearly from 0.93 at the flow channel side to the 0.8 at membrane side in z-direction of electrode. Gradient electrode structures in y- and x-direction have the same setting in their both positive and negative electrodes.

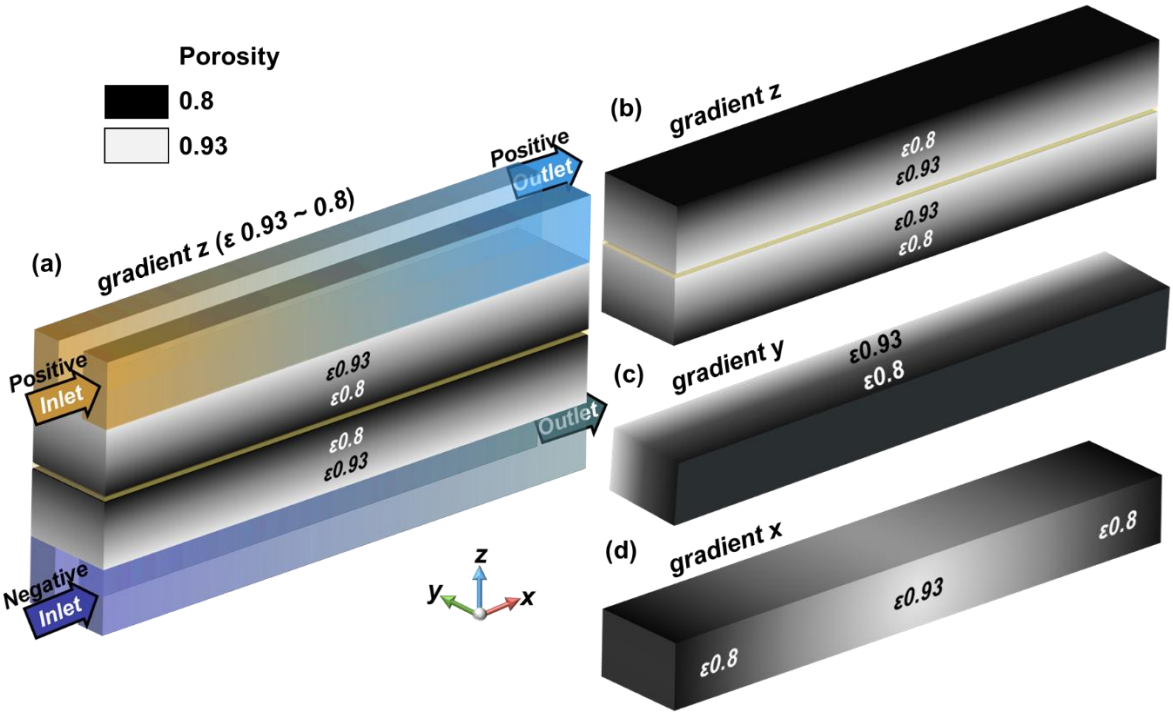

Fig.4 Structures of VRFB with different gradient electrodes, linear decreasing (a) and linear increasing (b) porosity in z-direction, linear increasing porosity in y-direction (c), and half linear increasing half decreasing porosity in x-direction (d).

3. Results and discussion

3.1 Effects of operating condition over a wide range of working temperature

First, a base case is calculated to give a holistic description of the distribution of velocities, current densities, and concentrations throughout the entire VRFB at various temperatures. Simulation results are shown in Fig.5 and the detailed electrode parameters are listed in Table 3. It is worth noting that the unmarked and unexplained parameters in following parametric studies are all subject to the parameters in basic case (Table 3). In addition, all contours are at the working potential 0.8 V.

Table 3 Electrode parameters of the base case.

Parameters	Symbols (Unit)	Value
ε	Electrode porosity	0.9
d_f	Carbon electrode fibre diameter (μm)	10

$thick_e$	Electrode thickness (mm)	1
SOC_{in}	SOC of inlet	0.5
Q_{in}	Inlet flow rate ($ml \cdot min^{-1}$)	30

Due to the unconnected inflow and outflow channel of the interdigitated flow field, the electrolyte penetration is increased to enhance the convection in electrodes, which results in a better electrochemical performance than the serpentine flow field case. The more uniform species distribution and less pressure drop comes from the shorter inflow and outflow route in the interdigitated flow field [36]. From the Fig.5 (a), (c) and (e), it is found that the velocity distribution: 1) almost same at different temperatures due to the property of interdigitated flow field; 2) highest value near inlet and outlet; 3) its value close to zero near both ends wall. The surface concentration distributions of V^{5+} in positive electrode and V^{2+} in negative electrode illustrates symmetry and show negligible variation along channel in x-direction. At the same working voltage, the surface concentration of reactants decreases with increased temperature. Fig.5 (b), (d) and (f) exhibit the current density distribution at the middle cross section of membrane in xy-plane with different colour legends and local current density distribution in yz-planes with same colour legend. It is obvious that, at a higher temperature, VRFB can attain a larger current density, which shows an asymmetrical distribution in all xyz-directions.

It is worth noting that in the following parametric studies, unless otherwise noted, all contours of velocity distribution, concentration distribution and current density distribution in yz-plane are set at the middle of channel length (x=8 mm). In addition, the velocity components in yz-direction are all scaled up by a factor of 50.

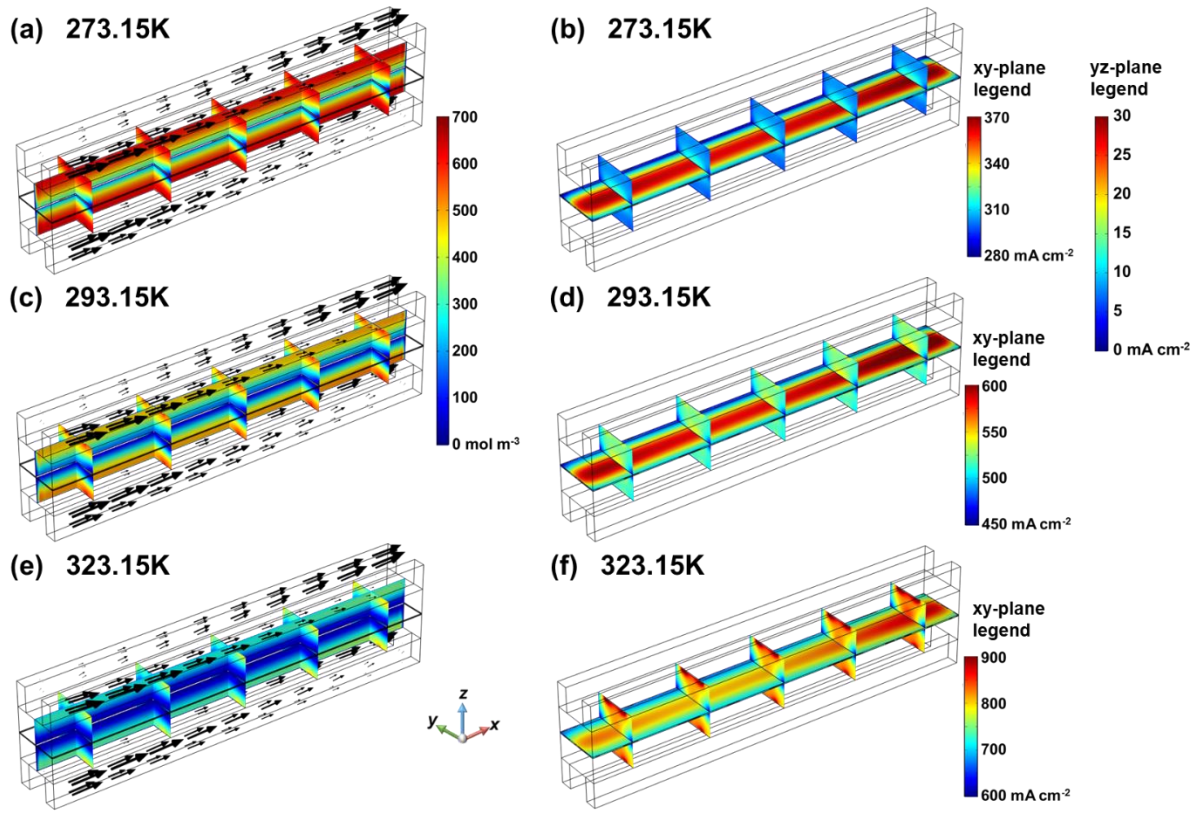

Fig.5 Surface concentrations distribution of the reactants in yz- and xz-planes with velocity vector at different temperatures (a), (c) and (e); Current density distribution at middle cross section of membrane in xy-plane and local current density distribution in yz-planes at different temperatures (b), (d) and (f).

3.1.1 Inlet flow rate

The effects of inlet flow rate on the polarization curves at different temperatures are shown in Fig.6 (a-c). With the increase of inlet flow rate, the battery performances at different temperatures are all improved. However, the performance improvement becomes more obvious with increased working temperature, due to the enhanced reactivity. It can be observed that, at a low inlet flow rate, the limiting current densities at different temperatures are all around 425 mA cm^{-2}. Nevertheless, the concentration loss increases with the increasing temperature. According to Eq. (5) and (7), as the viscosity of the negative electrolyte is larger than that of the positive electrolyte, the pressure drop of the negative electrode is larger than that of the positive electrode in Fig.6 (d), indicating a higher pump energy consumption in the negative

electrode. The difference of pressure drop between the negative electrode and the positive electrode increases with the decreasing temperature. With the increase of flow rate, the increase in pressure drop is more obvious at 273.15 K than that at 323.15 K. Due to the high viscosity of the electrolyte at 273.15 K, how to balance battery performance and system pump consumption becomes an important indicator for evaluating of battery operation and design.

From the Fig.6 (e), the high-speed region locates under the rib, and the low-speed region appears under the channel. Due to the characteristics of the interdigitated flow field analysed above, there is no significant difference between the velocity fields at 323.15 K and 273.15 K. While the main difference lies in the pressure drop, which will not be repeated in the following sections. Combining Fig.6 (f) and (g), the reactants are significantly consumed due to the faster electrochemical reaction at 323.15 K. The range of bulk concentration is 503~750 mol m^{-3} at 323.15 K and 638~750 mol m^{-3} at 273.15 K. The conversion of reactant at 323.15 K is higher and the bulk concentration decreases near the outlet channel. Moreover, the surface concentration of reactant on electrode fibre is much lower than its bulk concentration. The range of surface concentration is 24~437 mol m^{-3} at 323.15 K and 0.3~695 mol m^{-3} at 273.15 K. The distribution of surface concentration is related to the velocity distribution. For example, the surface concentration is close to zero in the low-speed region near the membrane under the flow channel. The distribution of local current density also shows a correlation with the velocity distribution and surface concentration distribution in Fig.6 (h). The local current density increases with the increasing temperature. The local current density is high at the rib edge and is small in the low-speed region near the membrane under the channel.

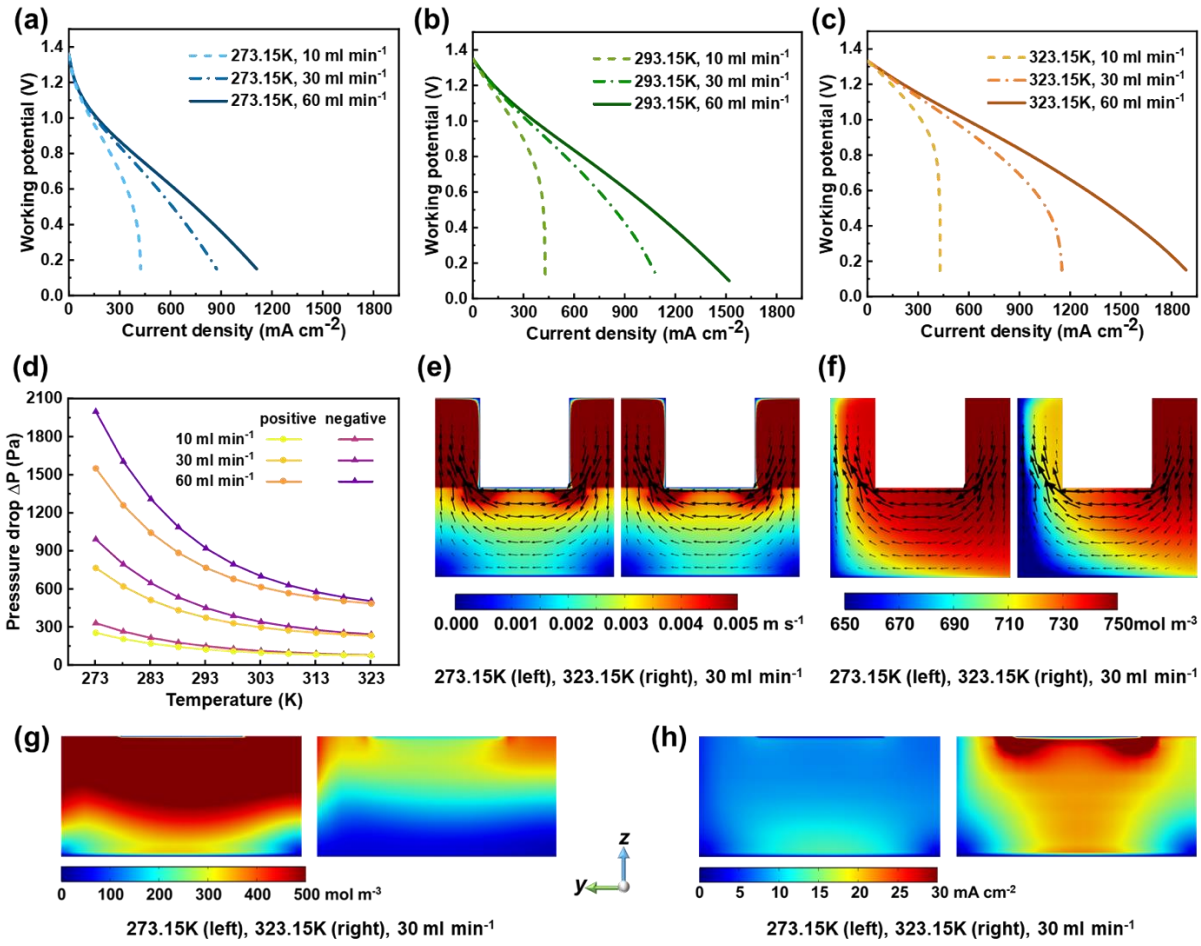

Fig.6 Polarization curves with different inlet flow rate at different temperatures (a-c); Pressure drop with temperature effects (d); Velocity distribution (e), V^{5+} bulk concentration distribution (f) with velocity component in yz-direction, V^{5+} surface concentration distribution (g), and local current density distribution (h).

3.1.2 Inlet SOC

The effects of inlet SOC on the polarization curves at different temperatures are shown in Fig.7 (a-c). Referred to the Eq.(28-31), OCV of battery varies with the different inlet SOCs and temperatures. As shown in Fig.7 (d), with increasing inlet SOC, the surface concentration can be increased, indicating a reduced concentration overpotential. Combining with Fig.7 (e), as the working temperature increases, the reactivity of electrochemical reaction also increases, leading to a high reactant consumption and a high local current density. However, according to Eq.(42), the mass transfer coefficient is only proportional to $|\vec{u}|^{0.9}$. As analysed above, the

difference in velocity field is negligible at various working temperatures. Therefore, with the increase of inlet SOC, the surface concentration of reactant decreases due to the limited mass transfer coefficient. In addition, the effects of concentration overpotential increases with the increasing working temperature. Noteworthy, with the decreasing working temperature, the ohmic overpotential and activation overpotential increase. The increased ohmic overpotential results from the reduced electrolyte conductivity according to Eq. (21) and (22). Additionally, the increased activation overpotential results from the reduced reaction rate constant based on Eq. (40) and (41). Therefore, even providing a high inlet SOC, these two dominant overpotentials still significantly limit the VRFB performance.

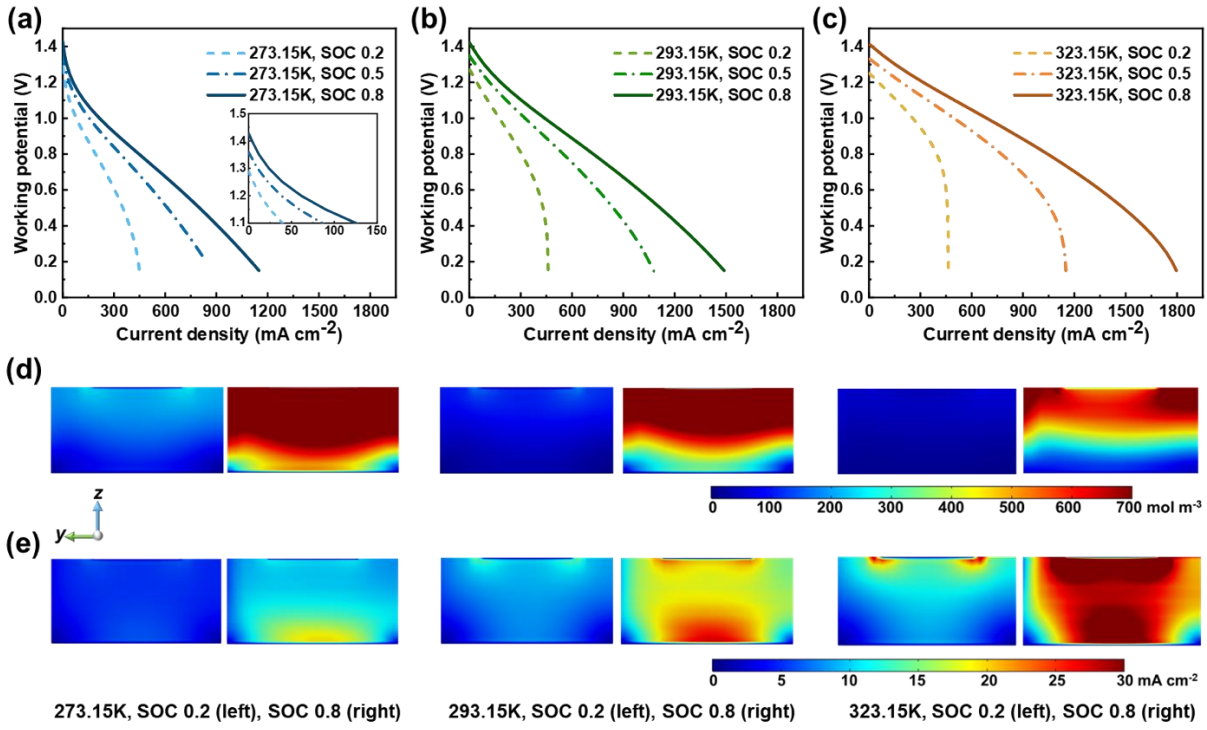

Fig.7 Polarization curves with different inlet SOC at different temperatures (a-c); V^{5+} surface concentration distribution (d), and local current density distribution (e).

3.2 Effects of electrode structure over a wide range of working temperature

Over a wide range of working temperature, the effect of electrode structure properties on battery performance demonstrates more complex trends than those of operating parameters.

The effects of electrode structure properties, such as porosity, fibre diameter and thickness, on battery performance over a wide range of working temperature are explored in this section.

3.2.1 Electrode porosity

The effects of electrode porosity on the polarization curves at different temperatures are shown in Fig.8 (a-c). As the porosity decreases, the improvement of battery performance becomes more significant at a higher temperature. The decreased porosity leads to a larger specific surface area, reducing the activation overpotential. According to Eq. (17) and (18), the decreased porosity can also reduce the ohmic overpotential, since total battery conductivity is increased (the increased effective electronic conductivity is larger than the decreased effective ionic conductivity).

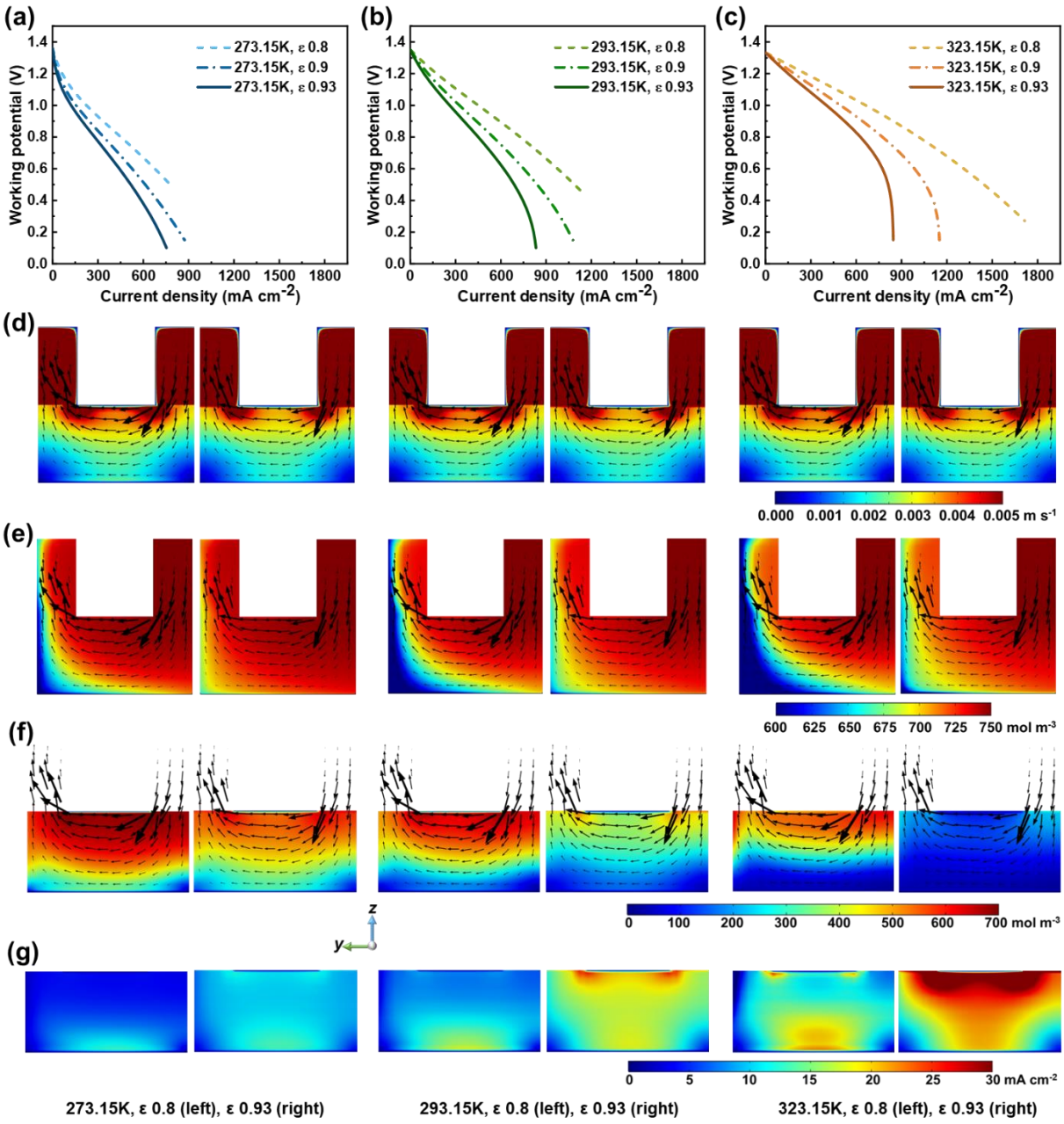

Fig.8 Polarization curves with different porosity electrode at different temperatures (a-c); Velocity distribution (d), V^{5+} bulk concentration distribution (e), V^{5+} surface concentration distribution (f), and local current density distribution (g).

From Fig.8 (d), compared with case of ε=0.93, the high-speed region under the rib at ε=0.8 is larger. In addition, the deviation between the velocity fields of ε=0.93 and ε=0.8 in a VRFB with interdigitated flow field is not obvious. The bulk concentration in ε=0.8 case is less uniform than that in ε=0.93 case, since more reactants are consumed (shown in Fig.8 (e)).

Moreover, with the increase of temperature, the difference of bulk concentration between ε=0.93 case and ε=0.8 case becomes more obvious. As mentioned above, the surface concentration of reactant is significantly lower than the bulk concentration of reactant and the minimum value is almost zero near the membrane under the flow channel, as demonstrated in Fig.8 (f).

Combining with Fig.8 (g), at the same operating voltage, although the current density of the battery with ε=0.93 is smaller than that of the battery with ε=0.8, the local current density in the electrode with ε=0.93 is larger than that in the electrode with ε=0.8. This can be explained by the insufficient specific surface area in the electrode with ε=0.93, according to Eq. (9), (24) and (25). Due to the limited mass transfer, the surface concentration of reactants is significantly lower than the bulk concentration in the electrode with ε=0.93, leading to a high concentration overpotential. With the increasing working temperature, the difference of surface concentration between ε=0.93 case and ε=0.8 case becomes more pronounced.

3.2.2 Electrode fibre diameter

Due to assembly problems such as sealing and mechanical strength, carbon-based electrodes are not easy to maintain a high porosity in the VRFB. Adjusting electrode fibre diameter is one of the methods to change electrode microstructural properties such as permeability and specific surface area. The effects of electrode fibre diameter on the polarization curves at different temperatures are shown in Fig.9 (a-c). To some extent, the effects of fibre diameter on battery performance are similar to the effects of porosity. Moreover, the decreased fibre diameter can result in an increase in the specific surface area, but does not have a direct impact on the battery conductivity. Combining Fig.9 (d) and (e), at the same operating voltage, although the current density of the battery with d_f =20 μm is smaller than that of the battery with d_f =5 μm, the local current density in electrode with d_f =20 μm is larger than that in electrode with d_f =5 μm. This can be explained by the insufficient specific surface area in the electrode with d_f =20 μm,

according to Eq. (9), (24) and (25). Due to the considerably limited mass transfer, the surface concentration of reactants is significantly lower than the bulk concentration in the electrode with d_f =20 μm, leading to a high concentration overpotential. With the increasing working temperature, the difference of surface concentration between d_f =20 μm case and d_f =5 μm case becomes more pronounced.

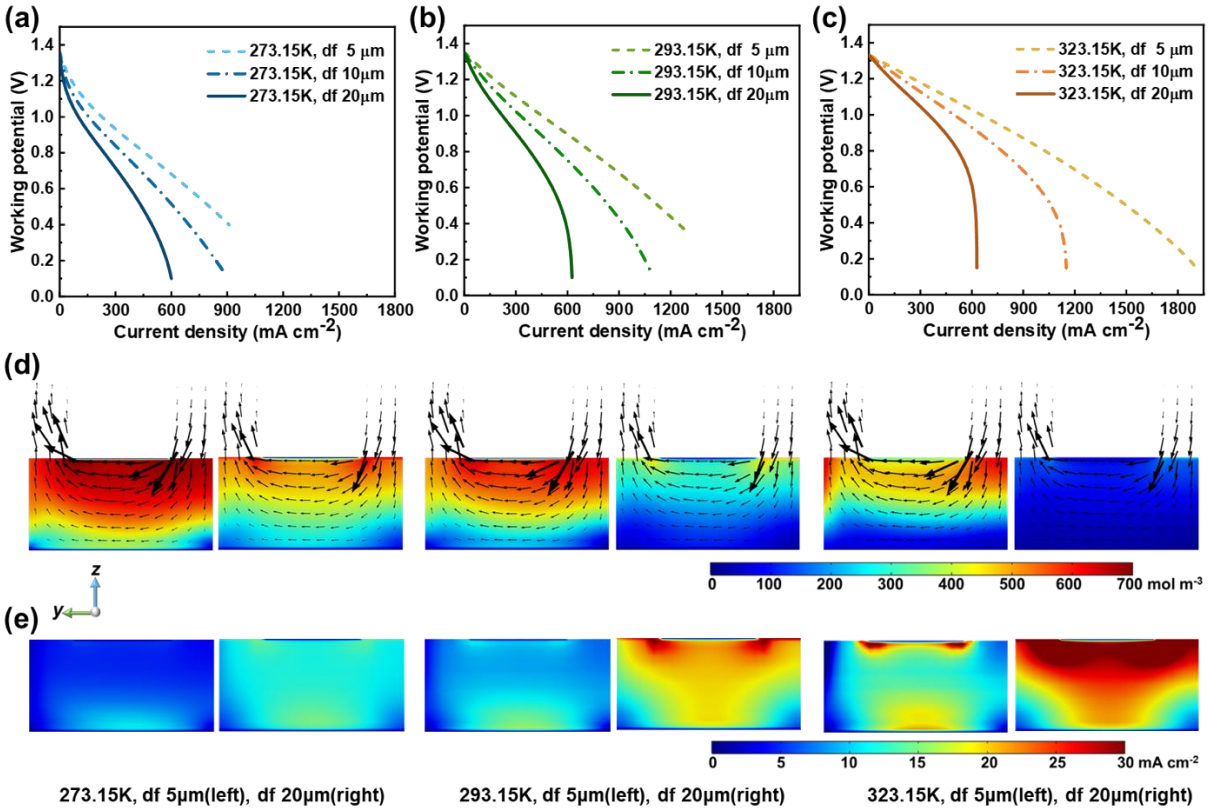

Fig.9 Polarization curves with different fibre diameter electrode at different temperatures (a-c); V^{5+} surface concentration distribution (d) and local current density distribution (e).

3.2.3 Electrode thickness

The effects of electrode thickness on the polarization curves at different temperatures are shown in Fig.10 (a-c). The VRFBs with different thick electrodes perform differently at different temperatures. At 273.15 K, when the working voltage < 0.9 V, the VRFB with a thinner electrode performs worse due to a higher activation overpotential. This can be explained by insufficient reaction sites in thin electrodes. At 273.15 K, with the further decrease

of working voltage, the VRFB with a thin electrode performs better than the VRFB with a thick electrode, since the ohmic overpotential in a thin electrode is smaller than that in a thick electrode. However, since the electrolyte ionic conductivity increases with the increasing temperature, the difference between the VRFB with a thin electrode and the VRFB with a thick electrode becomes smaller. Specifically, at 323.15 K, the effect of electrode thickness on battery performance is not obvious when the operating voltage is > 1.15 V. Additionally, with a further decrease in voltage at 323.15 K, the VRFB with a thin electrode performs better until the voltage decreases to 0.7 V. Interestingly, it is found that the performance of a VRFB with a thin electrode significantly decreases when the operating voltage is less than 0.7 V. Significant concentration overpotential in the thin electrode reduces the performance of VRFB. Limited by the insufficient total surface area of the 0.5 mm thick electrode, the limiting current densities of the VRFBs at different temperatures are all around 950 mA cm^{-2}.

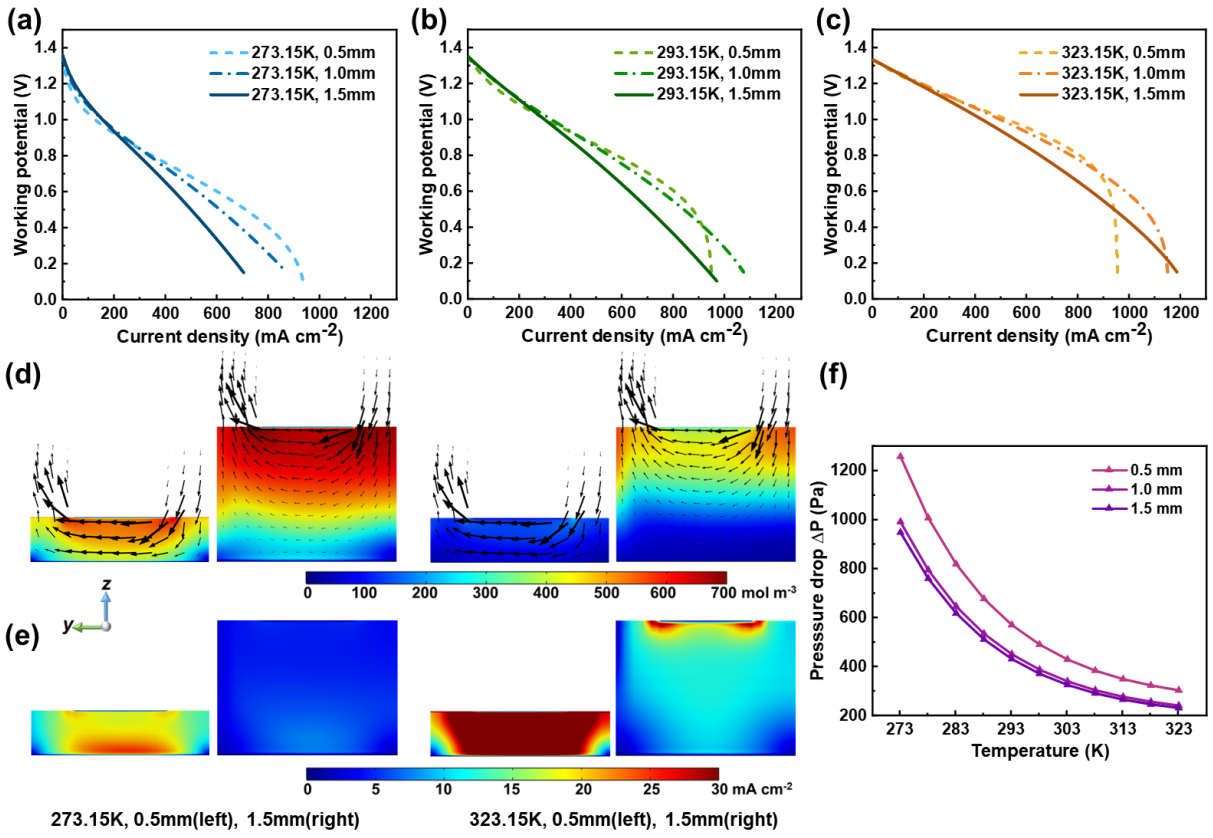

Fig.10 Polarization curves with different thickness electrode at different temperatures (a-c); V^{5+} surface concentration distribution (d) and local current density distribution (e); Pressure drops with temperature effects in negative sides (f).

Over a wide temperature range, the VRFB with a thin electrode shows an evident concentration overpotential. Combining Fig.10 (d) and (e), at 0.8 V, the surface concentration of reactant in a 0.5 mm thick electrode is lower than that in a 1.5 mm thick electrode at all temperatures. Furthermore, at 0.8 V, the local current density in a 0.5 mm thick electrode is higher than that in a 1.5 mm thick electrode at all temperatures. To achieve the same total current density, since the total reaction site (surface area) in a 0.5 mm thick electrode is less than that of a 1.5 mm thick electrode, the local current density in a 0.5 mm thick electrode needs to be higher, leading to a higher consumption of reactants on fibre surface.

In addition, with the increasing temperature, electrochemical activities and ionic conductivities both increase. Therefore, the activation and ohmic overpotentials decrease correspondingly. However, the local current density increases with the increasing temperature as well, leading to a significant decrease in the surface concentration of reactant on carbon fibre. With the decrease of electrode thickness, the velocity in the electrode becomes higher and distributes more uniform (Fig.10 (d)), also leading to a higher pressure drop (Fig.10 (f)). In Fig.10 (d), the velocity in a 1.5 mm thick electrode under the rib region is much higher than the velocity near membrane, which leads to a considerable non-uniform distributions of surface concentration of reactant and the local current density. Fig.10 (f) also indicates that, with the increasing electrode thickness, the pressure drop in a VRFB with interdigitated flow field decreases but remains nearly unchanged when the thickness is above 1 mm.

3.3 Effects of gradient electrode design over a wide range of working temperature

In the above results, VRFBs with various electrode structures behave differently with the increasing temperature. Some studies [6,37,38] apply gradient electrode design to improve

performance of VRFBs, so how the gradient electrode design affects the performance of a VRFB with interdigitated flow filed over a wide working temperature range is discussed in this section. The details of different gradient electrodes setting are illustrated in Fig.4.

3.3.1 Gradient porosity electrode design

The effects of different gradient porosity electrode design in z-direction on the polarization curves at various temperatures are shown in Fig.11 (a-c). All VRFBs with various linearly increased porosity perform almost as well as VRFB with a porosity 0.8. At 273.15 K, the electrode with a linearly increased porosity (0.8~0.9) performs slightly better (951.94 mA cm^{-2} at 0.35 V) even with less total surface area and low total conductivity compared to lower porosity gradient. At 323.15 K, the electrode with linearly increased porosity (0.8~0.85) performs better (1034.9 mA cm^{-2} at 0.8 V and 1843.8 mA cm^{-2} at 0.15 V). Fig.11 (d) shows that, at 0.8 V, the surface concentration of reactant in the electrode with linearly decreased porosity is lower than the surface concentration of reactant in the electrode with linearly increased porosity. Fig.11 (e) reveals the high local current density in both gradient electrodes occurs at high porosity region where the velocity is also high to ensure an adequate surface concentration of reactants. In the electrode with linearly decreased porosity, high velocity region only appears under rib and far away from membrane, leading to a large concentration overpotential near membrane. In contrast, the permeability of electrode with linearly increased porosity increases gradually along the electrode thickness, delivering a more uniform distribution of velocity in the electrode. The high velocity and local current density regions are close to the membrane, and there is no large area of near to zero local current density in electrode. As shown in Fig.11 (f), the different electrode structures can also affect the pump loss in VRFBs to further influence the overall efficiency of the VRFB system. Due to the high viscosity of the electrolytes at low temperature, the pressure drop response to different electrode design is also greater than that at high temperature. When the operating voltage > 0.5

V, the gradient porosity electrode (0.8~0.93) has a similar electrochemical output to an electrode with porosity of 0.8, whereas the pressure drop of the gradient porosity electrode is reduced by 40%. Noteworthy, with the increase of working temperature, more pumping energy can be saved in a gradient electrode (saving 1573.8 Pa at 273.15 K, 706.9 Pa at 293.15 K and 369.4 Pa at 323.15 K). To obtain both high VRFB performance and system efficiency, a careful and decent balance should be achieved between overpotentials and pump loss.

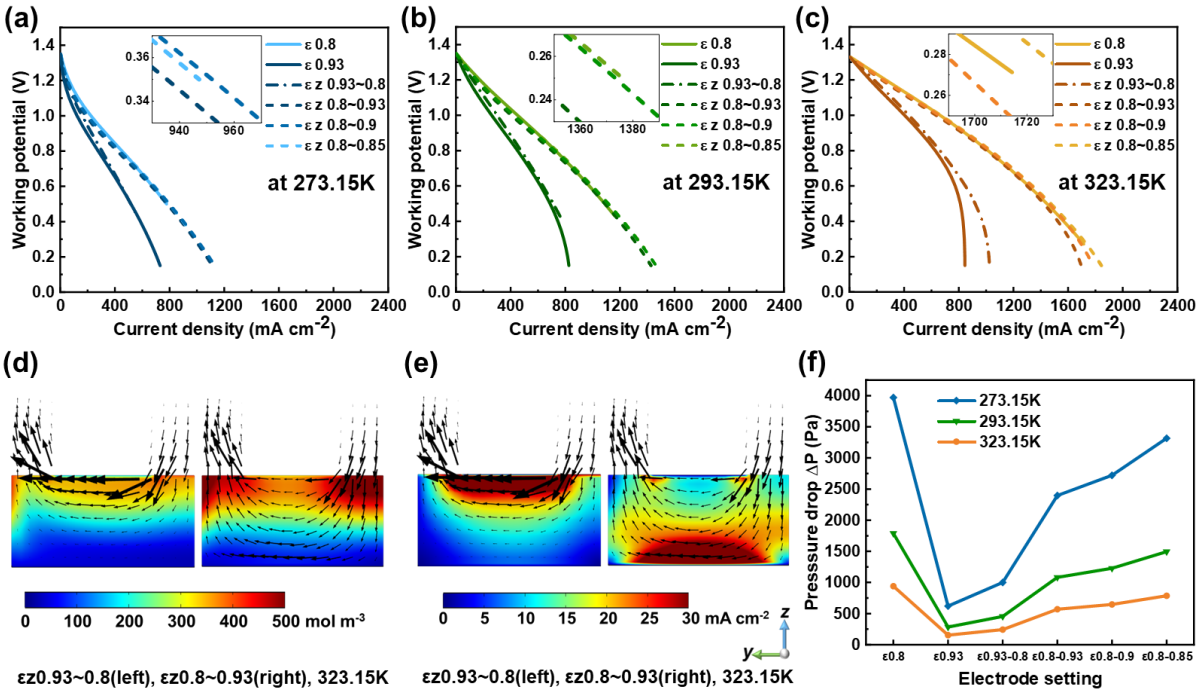

Fig.11 Polarization curves with different gradient porosity electrode design in z-direction at different temperatures (a-c); V^{5+} surface concentration distribution (d) and local current density distribution (e); Pressure drops in negative sides (f).

The effects of different gradient porosity electrode designs in xyz-directions on the polarization curves at various temperatures are shown in Fig.12 (a-c). Interestingly, the gradient porosity design in the z-direction has the most obvious improvement on the battery performance. Fig.12 (d) shows that the current density distribution has a highly coupled relation with the velocity distribution near membrane. The pressure drop in Fig.12 (e) shows similar results. Compared

with other electrode designs, the gradient porosity electrode design in x-direction has the least pump loss.

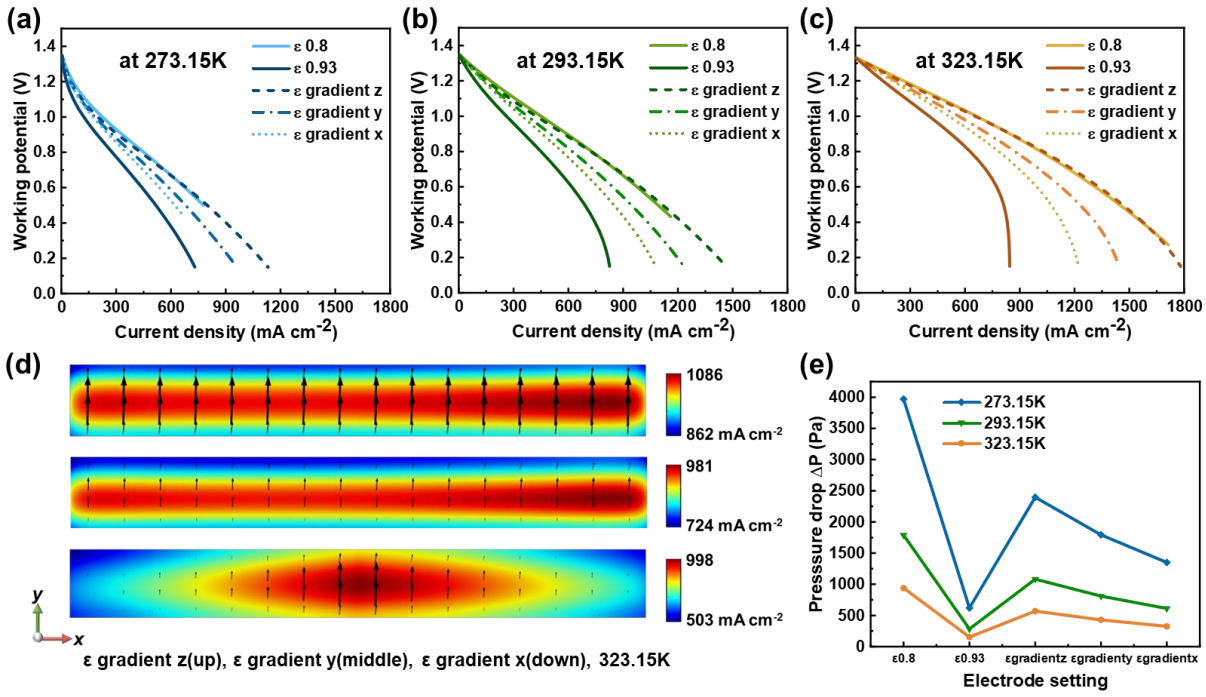

Fig.12 Polarization curves with gradient porosity electrode design in different direction at different temperatures (a-c); Current density distribution at middle cross section of membrane in xy-plane with velocity component (scale-up factor 150) in xy-direction at 0.05 mm from the membrane xy-plane of positive electrode (d); Pressure drops in negative sides (e).

3.3.2 Gradient fibre diameter electrode design

By using electrospinning method, a gradient in the fibre diameter can be created in the electrode [39]. The effects of electrodes with different gradient diameter fibres on the polarization curves at various temperatures are shown in Fig.13 (a-c). The bulk concentration in Fig.13 (d) reveals a higher reactant conversion rate near the flow outlet in an electrode with gradient diameter (5~10 μm) fibre. Combining Fig.13 (e) and (f), the surface concentration of the reactant is smaller in an electrode with gradient diameter (5~20 μm) fibre. However, with a smaller total surface area, the electrode gradient diameter (5~20 μm) fibre has a lower current density than the electrode with gradient diameter (5~10 μm) fibre. The electrode design with gradient

diameter fibre design can also help decrease the pressure drop in VRFB as shown in Fig.13 (g). In conclusion, by sacrificing a little VRFB's performance, the electrode with gradient diameter (5~10 μm) fibre only achieves 68% of the pressure drop of electrode with constant diameter (5 μm) fibre over a wide working temperature range.

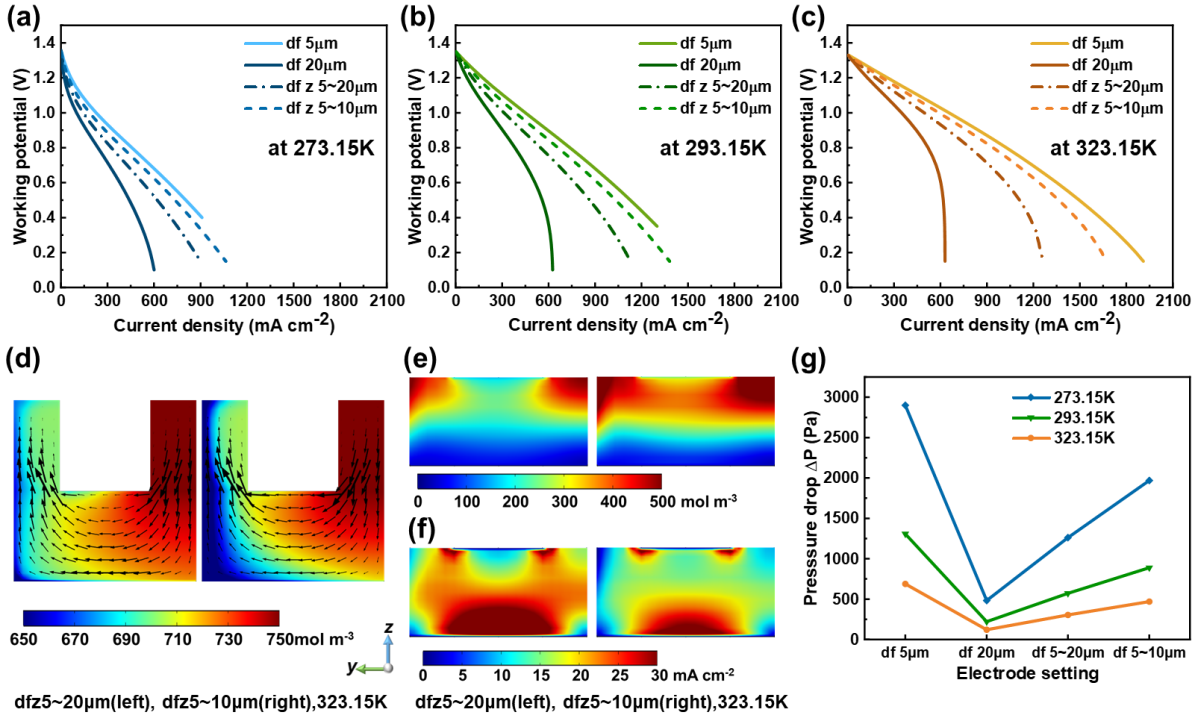

Fig.13 Polarization curves with different gradient fibre diameter electrode design in z-direction at different temperatures (a-c); V^{5+} bulk concentration distribution (d), V^{5+} surface concentration distribution (e) and local current density distribution (f); Pressure drops in negative sides (g).

4. Conclusion

In this work, to reveal the effects of working temperature on the battery performance and electrode optimization design of VRFB, a numerical 3D model is developed to simulate the coupled physical/ electrochemical processes in a VRFB with interdigitated flow field. The fluid flow, species transport, charge transport, and electrochemical reactions behaviours at different temperatures are fully considered. The model shows a good agreement with the experimental data from the literature. The effects of operating conditions (inlet flow rate and SOC) and

electrode structural parameters (porosity, fibre diameter and thickness) on the VRFB performance are well-studied over a wide range of working temperature. Meanwhile, the effects of different gradient electrode designs on the performance of VRFB are also discussed in detail over a wide range of working temperature.

Increasing the inlet flow rate and SOC can both improve the battery performance. However, increased inlet flow rate results in a significant pressure loss, especially at a low temperature, subsequently reducing the overall efficiency of the system. Reducing the porosity to 0.8 or fibre diameter to 5 μm not only increases the performance of VRFB, but also increases the pump consumption. At a low temperature, thin electrode performs better when the working potential < 0.9 V. At a high temperature, thin electrode performs better when the working voltage > 0.7 V. It shows the effects of a wide working temperature range on the electrode thickness optimization.

The gradient electrode design is applied for balancing the battery performance and pump loss. When the operating voltage > 0.5 V, the gradient porosity electrode (0.8~0.93) has a similar electrochemical output to an electrode with porosity of 0.8, whereas the pressure drop is reduced by 40% at all temperature. The gradient porosity design in the z-direction has the most significant improvement on the battery performance at all temperature. By sacrificing a little VRFB's performance, the pressure drop of the gradient electrode with gradient diameter (5~10 μm) fibre reduces 32%, compared to electrode with constant diameter (5 μm) fibre.

Overall, this work provides insights into the effects of a wide temperature range on the VRFB's performance and can serve as a useful toolkit for further large-scale VRFB system optimization, including operation optimization, flow pattern optimization, and electrodes optimization.

Acknowledgments

This research is supported by a grant under the Theme-based Scheme (project number: T23–601/17-R) from Research Grants Council, University Grants Committee, Hong Kong SAR.

References

[1] Yu J, He Q, Yang G, Zhou W, Shao Z, Ni M. Recent Advances and Prospective in Ruthenium-Based Materials for Electrochemical Water Splitting. ACS Catal 2019;9:9973–10011. https://doi.org/10.1021/acscatal.9b02457.

[2] Li Z, Zhang H, Xu H, Xuan J. Advancing the multiscale understanding on solid oxide electrolysis cells via modelling approaches: A review. Renewable and Sustainable Energy Reviews 2021;141. https://doi.org/10.1016/j.rser.2021.110863.

[3] Li Z, He Q, Wang C, Xu Q, Guo M, Bello IT, et al. Ethylene and power cogeneration from proton ceramic fuel cells (PCFC): A thermo-electrochemical modelling study. J Power Sources 2022;536. https://doi.org/10.1016/j.jpowsour.2022.231503.

[4] Zhao D, Xia Z, Guo M, He Q, Xu Q, Li X, et al. Dynamic hierarchical modeling and control strategy of high temperature proton exchange electrolyzer cell system. Int J Hydrogen Energy 2022;47:22302–15. https://doi.org/10.1016/j.ijhydene.2022.05.067.

[5] Chen Z, Liu Y, Yu W, He Q, Ni M, Yang S, et al. Cost evaluation and sensitivity analysis of the alkaline zinc-iron flow battery system for large-scale energy storage applications. J Energy Storage 2021;44:103327. https://doi.org/10.1016/j.est.2021.103327.

[6] He Q, Yu J, Guo Z, Sun J, Zhao S, Zhao T, et al. Modeling of Vanadium Redox Flow Battery and Electrode Optimization with Different Flow Fields. E-Prime 2021:100001. https://doi.org/10.1016/j.prime.2021.100001.

[7] Xiao S, Yu L, Wu L, Liu L, Qiu X, Xi J. Broad temperature adaptability of vanadium redox flow battery - Part 1: Electrolyte research. Electrochim Acta 2016;187:525–34. https://doi.org/10.1016/j.electacta.2015.11.062.

[8] Xi J, Xiao S, Yu L, Wu L, Liu L, Qiu X. Broad temperature adaptability of vanadium redox flow battery - Part 2: Cell research. Electrochim Acta 2016;191:695–704. https://doi.org/10.1016/j.electacta.2016.01.165.

[9] Zhang C, Zhao TS, Xu Q, An L, Zhao G. Effects of operating temperature on the performance of vanadium redox flow batteries. Appl Energy 2015;155:349–53. https://doi.org/10.1016/j.apenergy.2015.06.002.

[10] Yin S, Zhou L, Du X, Yang Y. Influence of temperature on performance of all vanadium redox flow battery: analysis of ionic mass transfer. Ionics (Kiel) 2019;25:593–606. https://doi.org/10.1007/s11581-018-2626-z.

[11] Parasuraman A, Lim TM, Menictas C, Skyllas-Kazacos M. Review of material research and development for vanadium redox flow battery applications. Electrochim Acta 2013;101:27–40. https://doi.org/10.1016/j.electacta.2012.09.067.

[12] Corcuera S, Skyllas-Kazacos M. State-of-charge monitoring and electrolyte rebalancing methods for the vanadium redox flow battery. European Chemical Bulletin 2012;1:511–9. https://doi.org/10.17628/ECB.2012.1.511-519.

[13] Ressel S, Bill F, Holtz L, Janshen N, Chica A, Flower T, et al. State of charge monitoring of vanadium redox flow batteries using half cell potentials and electrolyte density. J Power Sources 2018;378:776–83. https://doi.org/10.1016/j.jpowsour.2018.01.006.

[14] Kim D, Jeon J. A high-temperature tolerance solution for positive electrolyte of vanadium redox flow batteries. Journal of Electroanalytical Chemistry 2017;801:92–7. https://doi.org/10.1016/j.jelechem.2017.07.037.

[15] Xi J, Jiang B, Yu L, Liu L. Membrane evaluation for vanadium flow batteries in a temperature range of −20–50 °C. J Memb Sci 2017;522:45–55. https://doi.org/10.1016/j.memsci.2016.09.012.

[16] Rao P, Jayanti S. Influence of electrode design parameters on the performance of vanadium redox flow battery cells at low temperatures. J Power Sources 2021;482. https://doi.org/10.1016/j.jpowsour.2020.228988.

[17] Ishitobi H, Saito J, Sugawara S, Oba K, Nakagawa N. Visualized cell characteristics by a two-dimensional model of vanadium redox flow battery with interdigitated channel and thin active electrode. Electrochim Acta 2019;313:513–22. https://doi.org/10.1016/j.electacta.2019.04.055.

[18] Zheng Q, Zhang H, Xing F, Ma X, Li X, Ning G. A three-dimensional model for thermal analysis in a vanadium flow battery. Appl Energy 2014;113:1675–85. https://doi.org/10.1016/j.apenergy.2013.09.021.

[19] Oh K, Yoo H, Ko J, Won S, Ju H. Three-dimensional, transient, nonisothermal model of all-vanadium redox flow batteries. Energy 2015;81:3–14. https://doi.org/10.1016/j.energy.2014.05.020.

[20] Al-Fetlawi H, Shah AA, Walsh FC. Non-isothermal modelling of the all-vanadium redox flow battery. Electrochim Acta 2009;55:78–89. https://doi.org/10.1016/j.electacta.2009.08.009.

[21] Wei Z, Zhao J, Skyllas-Kazacos M, Xiong B. Dynamic thermal-hydraulic modeling and stack flow pattern analysis for all-vanadium redox flow battery. J Power Sources 2014;260:89–99. https://doi.org/10.1016/j.jpowsour.2014.02.108.

[22] Trovò A, Saccardo A, Giomo M, Guarnieri M. Thermal modeling of industrial-scale vanadium redox flow batteries in high-current operations. J Power Sources 2019;424:204–14. https://doi.org/10.1016/j.jpowsour.2019.03.080.

[23] Wang H, Soong WL, Pourmousavi SA, Zhang X, Ertugrul N, Xiong B. Thermal dynamics assessment of vanadium redox flow batteries and thermal management by active temperature control. J Power Sources 2023;570:233027. https://doi.org/10.1016/j.jpowsour.2023.233027.

[24] Wang S, Fan Y, Jin S, Takyi-Aninakwa P, Fernandez C. Improved anti-noise adaptive long short-term memory neural network modeling for the robust remaining useful life prediction of lithium-ion batteries. Reliab Eng Syst Saf 2023;230:108920. https://doi.org/10.1016/j.ress.2022.108920.

[25] Wang S, Takyi-Aninakwa P, Jin S, Yu C, Fernandez C, Stroe DI. An improved feedforward-long short-term memory modeling method for the whole-life-cycle state of charge prediction of lithium-ion batteries considering current-voltage-temperature variation. Energy 2022;254:124224. https://doi.org/10.1016/j.energy.2022.124224.

[26] Xu J, Ma Q, Xing L, Li H, Leung P, Yang W, et al. Modeling the effect of temperature on performance of an iron-vanadium redox flow battery with deep eutectic solvent (DES) electrolyte. J Power Sources 2020;449:227491. https://doi.org/10.1016/j.jpowsour.2019.227491.

[27] Chen W, Kang J, Shu Q, Zhang Y. Analysis of storage capacity and energy conversion on the performance of gradient and double-layered porous electrode in all-vanadium redox flow batteries. Energy 2019;180:341–55. https://doi.org/10.1016/j.energy.2019.05.037.

[28] Zhou XL, Zhao TS, An L, Zeng YK, Yan XH. A vanadium redox flow battery model incorporating the effect of ion concentrations on ion mobility. Appl Energy 2015;158:157–66. https://doi.org/10.1016/j.apenergy.2015.08.028.

[29] Sun J, Zheng M, Yang Z, Yu Z. Flow field design pathways from lab-scale toward large-scale flow batteries. Energy 2019;173:637–46. https://doi.org/10.1016/j.energy.2019.02.107.

[30] Zhou XL, Zhao TS, An L, Zeng YK, Wei L. Modeling of ion transport through a porous separator in vanadium redox flow batteries. J Power Sources 2016;327:67–76. https://doi.org/10.1016/j.jpowsour.2016.07.046.

[31] Tang A, Bao J, Skyllas-Kazacos M. Studies on pressure losses and flow rate optimization in vanadium redox flow battery. J Power Sources 2014;248:154–62. https://doi.org/10.1016/j.jpowsour.2013.09.071.

[32] Bhattarai A, Wai N, Schweiss R, Whitehead A, Lim TM, Hng HH. Advanced porous electrodes with flow channels for vanadium redox flow battery. J Power Sources 2017;341:83–90. https://doi.org/10.1016/j.jpowsour.2016.11.113.

[33] Lu MY, Deng YM, Yang WW, Ye M, Jiao YH, Xu Q. A novel rotary serpentine flow field with improved electrolyte penetration and species distribution for vanadium redox flow battery. Electrochim Acta 2020;361. https://doi.org/10.1016/j.electacta.2020.137089.

[34] Martin J, Schafner K, Turek T. Preparation of Electrolyte for Vanadium Redox-Flow Batteries Based on Vanadium Pentoxide. Energy Technology 2020;8. https://doi.org/10.1002/ente.202000522.

[35] Zhu S, Pelton RH, Collver K. Mechanistic modelling of fluid permeation through compressible fiber beds. Chem Eng Sci 1995; 50: 3557-3572. https://doi.org/10.1016/0009-2509(95)00205-J.

[36] Gostick JT, Fowler MW, Pritzker MD, Ioannidis MA, Behra LM. In-plane and through-plane gas permeability of carbon fiber electrode backing layers. J Power Sources 2006;162:228–38. https://doi.org/10.1016/j.jpowsour.2006.06.096.

[37] Carta R, Palmas S, Polcaro AM, Tola G. Behaviour of a carbon felt flow by electrodes Part I: Mass transfer characteristics. J Appl Electrochem 1991;21:793-798.

[38] Newman J, Thomas-Alyea KE. Electrochemical systems. John Wiley & Sons; 2012.

[39] Shah AA, Watt-Smith MJ, Walsh FC. A dynamic performance model for redox-flow batteries involving soluble species. Electrochim Acta 2008;53:8087–100. https://doi.org/10.1016/j.electacta.2008.05.067.

[40] AllenJ. Bard, Parsons R, Jordan J. Standard potentials in aqueous solution. CRC Press; 1985.

[41] You X, Ye Q, Cheng P. The Dependence of Mass Transfer Coefficient on the Electrolyte Velocity in Carbon Felt Electrodes: Determination and Validation. J Electrochem Soc 2017;164:E3386–94. https://doi.org/10.1149/2.0401711jes.

[42] Skyllas-Kazacos M, Rychick M, Robins R. All-vanadium redox battery. US Patent 4,786,567, 1988.

[43] Yamamura T, Watanabe N, Yano T, Shiokawa Y. Electron-transfer kinetics of Np3+/ Np4+, NpO2+/ NpO2 2+, V2+/ V3+, and VO2+/ VO2+ at carbon electrodes. J Electrochem Soc 2005;152:A830. https://doi.org/10.1149/1.1870794

[44] Sum E, Skyllas-Kazacos M. A study of the V (II)/V (III) redox couple for redox flow cell applications. J Power Sources 1985;15:179-190. https://doi.org/10.1016/0378-7753(85)80071-9

[45] Bromberger K, Kaunert J, Smolinka T. A Model for All-Vanadium Redox Flow Batteries: Introducing Electrode-Compression Effects on Voltage Losses and Hydraulics. Energy Technology 2014;2:64–76. https://doi.org/10.1002/ente.201300114.

[46] Houser J, Clement J, Pezeshki A, Mench MM. Influence of architecture and material properties on vanadium redox flow battery performance. J Power Sources 2016;302:369–77. https://doi.org/10.1016/j.jpowsour.2015.09.095.

[47] Jiang HR, Zhang BW, Sun J, Fan XZ, Shyy W, Zhao TS. A gradient porous electrode with balanced transport properties and active surface areas for vanadium redox flow batteries. J Power Sources 2019;440. https://doi.org/10.1016/j.jpowsour.2019.227159.

[48] Chen W, Kang J, Shu Q, Zhang Y. Analysis of storage capacity and energy conversion on the performance of gradient and double-layered porous electrode in all-vanadium redox flow batteries. Energy 2019;180:341–55. https://doi.org/10.1016/j.energy.2019.05.037.

[49] Sun J, Wu MC, Fan XZ, Wan YH, Chao CYH, Zhao TS. Aligned microfibers interweaved with highly porous carbon nanofibers: A Novel electrode for high-power vanadium redox flow batteries. Energy Storage Mater 2021;43:30–41. https://doi.org/10.1016/j.ensm.2021.08.034.